Proceedings of ASME Turbo Expo 2025
Turbomachinery Technical Conference and Exposition
GT2025
June 16-20, 2025, Memphis, Tennessee

GT2025-153967

A FRAMEWORK FOR COMPUTATIONAL DYNAMIC CHARACTERISATION OF DRY GAS SEALS FOR ASSESSING SYSTEM RESPONSE

Dimitrios Vitlaris[1], Jerry Thomas John[1], Mani Santhanakrishnan[1], David John Rajendran[1], Ioannis Roumeliotis[1], David Pickens III[2], Jasper Oranje[3],

[1]Centre for Propulsion and Thermal Power Engineering, Cranfield University, United Kingdom
[2]John Crane, Illinois, USA
[3]John Crane, London, United Kingdom

ABSTRACT

A computational framework to study the dynamic response of a dry gas seal (DGS) during multi-axis rotor vibrations is described in this work. The DGS comprises Rayleigh pads grooved in the primary ring and a pumping volume, and is used to explore the gas film behaviour for different rotor speeds and air supply pressures. Steady-state CFD simulations are conducted to determine the stiffness coefficients at various primary ring positions while the non-linear damping coefficients are computed from transient analyses. A novel methodology that allows the complete primary ring's movement is developed by specifying a wall motion through a transfer function. A mesh deformation strategy is established in which the grid is controlled using a Laplacian equation along with smoothing iterations, and differential, gradual steps of wall motion enable high-quality "real-time" simulations.

The gas film flow field is characterised by the generation of dynamic pressure from the Rayleigh pads and the flow entrapment in the pumping volume. The gas film thickness reduces circumferentially to reduce leakages thus improving the film stiffness. Higher gas film pressure is generated at higher air inlet pressures and rotor speeds, leading to an increase in stiffness coefficients. During the translational motion, the stiffness reduces as the film thickness increases while the damping response improves with the air inlet pressure. When the primary ring tilts, the stiffness and damping effects from the induced force in the radial direction are negligible. Negative stiffness and damping coefficients are also obtained, which have important implications for stable rotor operation. The computed opening forces depend on the primary ring's position and the effects of rotational speed and air supply pressure are highlighted. Finally, the calculated dynamic coefficients are utilised in a rotordynamics model to determine its dynamic response characteristics. This study proposes a numerical framework to accurately study the dynamic stability of DGSs that are working under harsh dynamic conditions, leading to better performance calculations and initial designs.

Keywords: dry gas seal, dynamic response, unsteady CFD

NOMENCLATURE

Roman letters

C_{ij}	Damping Coefficient [Ns/m]
f	Frequency [Hz]
$\vec{F}_i$	Spring force on mesh node [N]
$F_{x,p}$, $F_{y,p}$	Fluid force on perturbed position in x and y directions [N]
$F_{x,eq}$, $F_{y,eq}$	Fluid force on equilibrium position in x and y directions [N]
K_{ij}	Stiffness Coefficient [N/m]
k_{ij}	Spring stiffness of mesh node [N/m]
k_{fac}	Spring factor of mesh node [-]
L	Connecting rod length [m]
N	Shaft speed [% of max. rpm]
p	Air supply pressure [Pa]
p_{ref}	Reference pressure [Pa]
r_c	Crank radius [m]
r_{in}, r_{out}	Inner and outer seal radii [m]
x_i,x_j	Position of mesh nodes i,j [m]
x_{offset}	Primary wall offset [m]
x_p	Position of primary wall [m]

Greek letters

$\Delta\vec{x}_i$, $\Delta\vec{x}_j$	Displacement of nodes i and j [m]
Δx	Primary wall displacement [m]
$\dot{\Delta x}$	Primary wall velocity [m/s]
θ_c	Crank angle [degree]
θ_{dev}	Deviation angle from vertical plane [degree]
θ_{max}	Maximum deviation angle [degree]
ω	Angular frequency [Hz]
Ω	Angular Velocity [rad/s]

Abbreviations

CFD	Computational Fluid Dynamics

Copyright © 2025 by ASME;
reuse license CC-BY 4.0

DGS Dry Gas Seal
FSI Fluid-Structure Interaction
S-DGS Spiral-Grooved Dry Gas Seal
GCI Grid Convergence Index

1. INTRODUCTION

A Dry Gas Seal (DGS) is a mechanical seal commonly used for turbomachinery applications to reduce gas leakage under extreme conditions with a high degree of safety and reliability. Unlike the traditional oil film seals, DGS offer reduced friction and wear, increased efficiency, and are fitted to the majority of new compressors [1], [2]. This type of sealing system relies on a thin layer of gas to create a contactless, non-wearing barrier between a stationary primary ring and a rotating mating ring. The primary ring is typically manufactured using a carbon graphite material and is allowed to move axially where the opening force generated by the fluid film acts against the closing force of springs, which are connected to the primary ring. The mating ring is made of a harder material, namely silicon carbide or silicon nitride, and is mounted on a shaft sleeve that is constrained axially. At static conditions, the air supply creates a hydrostatic pressure that results in low startup torque and less parasitic power. When the shaft is rotating, a hydrodynamic pressure is induced that forces the primary ring to lift thus creating a running film gap. Conventional film gap values vary between 2.5 to 10 μm and depend on the seal pressure, the rotational speed of the mating ring, and the DGS configuration.

The spiral-grooved DGS (S-DGS) has been the focus of research for many years. Its performance and behaviour have been explored through computational methods and experimental campaigns. In detail, the influence of sealing pressure on key performance parameters has been investigated and it is reported that the leakage, opening force and gas film stiffness increase with the sealing pressure [3], [4], [5]. The fluid flow characteristics for various film thicknesses and flow regimes have been explored using computational models, and results indicated that the opening force decreases as the film thickness increases [6], [7], [8]. Moreover, the effect of groove ring rotation on sealing performance was examined by a thermal-fluid-structure interaction coupling method and results demonstrated that the gas film pressure and temperature values are higher in the grooved rotating ring than in the grooved stationary ring.

The self-regulation of the film gap in all operating conditions is a main characteristic of the DGS technology. Therefore, when designing dry gas seals, special attention is paid to ensuring that the required dynamic characteristics are provided. The dynamic response of seals plays a critical role in sealing performance and equipment reliability as airflow excitation, severe vibrations, and grinding can lead to gas film instabilities and friction-induced failures [9]. The stiffness and damping coefficients for different gas films and operating conditions have been calculated numerically by recent studies. The axial vibration of a seal was analysed under various operating points and the impact of the damping on the dynamic response of the DGS was obtained [10]. The gas film disturbance characteristics were studied by Yang et al. [11] in a high-speed, high-pressure S-DGS and results showed that large excitation amplitude and frequency strongly affect the leakage, while smaller gas film thickness oscillations are beneficial for a mating ring in a specific range of material densities. Moreover, the transient sealing performance of a hyperelliptic curve groove DGS was investigated and the influence of dynamic coefficients on dynamic tracking property was obtained [12]. However, the gas film is treated as a mass-spring-damper system in all previous studies where the Reynolds equation is utilised to obtain the pressure distribution with fixed stiffness and damping properties. Also, CFD investigations [13], [14] are focused on steady-state approaches that are sufficient for fixed operating conditions but neglect transient effects. The transient non-linear dynamic response of a DGS was studied using a transient CFD-FSI model and the importance of fluid gas modelling without the need to include analytical models is highlighted [15].

Therefore, the time-varying flow field effects computed by a transient CFD model, which cause the non-linear behaviour of dynamic coefficients, while the DGS is displaced both positional (translation) and angular (tilt) are described in this work. The motion of the primary walls in the film gap is achieved by implementing a computational method that uses a wall transfer function to mimic the translational and tilting movements along with a mesh deformation technique. The evolution of pressure, opening force, stiffness and damping coefficients are quantified and discussed in the paper. The hitherto unexplored behaviour of dynamic coefficients as computed by taking into account transient gas effects in this study, provides a computational framework to examine the dynamic response of DGS which can be used as a valuable tool during the design phase for investigating potential improvements in performance and seal stability.

2. MODEL DESCRIPTION

The dynamic coefficients are characterised using a DGS with Rayleigh pad configurations grooved in the primary ring. Air is supplied through a drilling orifice to a pumping volume surrounded by walls, which are named channel walls, and Rayleigh pads are grooved to the primary ring to provide greater film stiffness. Radial leakage is minimised by placing a small film gap, which acts as a circumferential dam, at the inner and outer radii. The model is shown in Figure 1.

3. COMPUTATIONAL SETUP

A 30-degree section is simulated to minimise computational cost, and a hybrid discretisation procedure is followed in which a structured mesh, which allows better control of points, is generated in key geometric areas such as sharp edges. The mesh is dominated by hexahedral elements and the addition of high-quality prismatic cells completes it. A rigorous grid sensitivity study was conducted in which three grids of different sizes were tested and the number of mesh points in the film gap was varied by keeping the maximum aspect ratio below 300. The grid refinement is based on the total element number and the refinement ratio is set to 1.5, while the largest surface element edge is determined from the maximum aspect ratio value. A total mesh of 13 million elements with 16 elements in the gas film and 30 in the pumping volume is finalised after a grid convergence study, based on the approach suggested by Roache [[16], indicated that the solution of local and global parameters is well within the asymptotic

Copyright © 2025 by ASME;
reuse license CC-BY 4.0

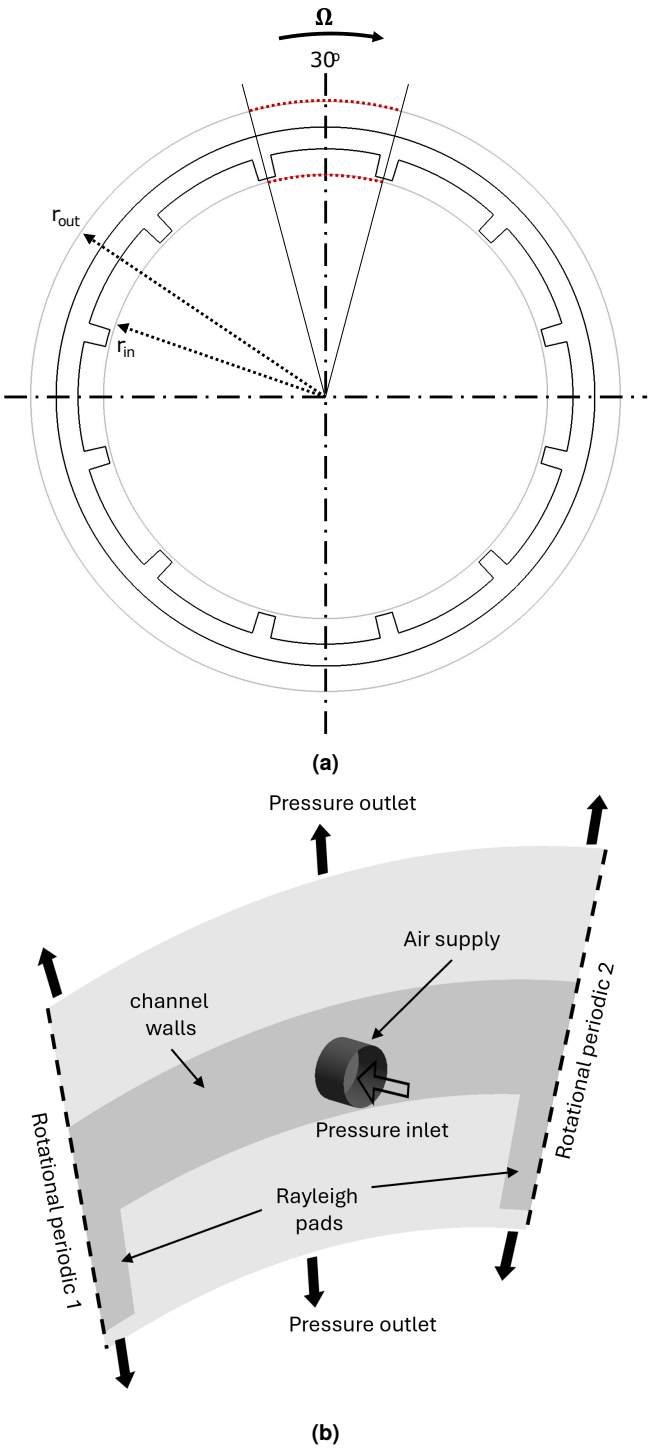


FIGURE 1: SCHEMATICS OF OF ENTIRE GEOMETRY (A) AND A 30° SECTOR SHOWING COMPONENT DETAILS, AND THE COMPUTATIONAL DOMAIN AND BOUNDARY CONDITIONS (B)

range with the Grid Convergence Index (GCI) values being no more than 1.5%. The computational model was also validated against experimental data provided by John Crane UK, where a DGS was examined in a test rig with thermocouples positioned at critical locations. The results showed good agreement in terms of leakage rates with the difference being within 4%. The dynamic flow field solutions are computed by the transient Navier-Stokes equations and the flow regime is considered to be laminar. This is explained based on the flow regimes between a rotating plane and a stationary disc that Brunetiere [17] highlighted in which the computed Re_c at the specified h/R fall within the laminar zone with merged boundary layers (I), as seen in Figure 2.

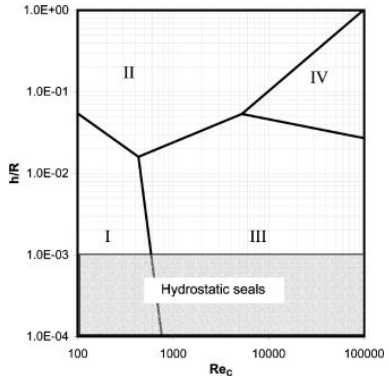


FIGURE 2: FLOW REGIMES BETWEEN A ROTATING AND A STATIONARY DISC [17].

A commercial, finite volume solver [18] is used with second-order schemes for the spatial discretisation of momentum and density equations and a second-order implicit scheme for the temporal derivatives. The PRESTO! scheme is used for the interpolation of pressure and the pressure-velocity coupling is achieved by the robust Coupled algorithm. Moreover, a temporal sensitivity analysis was conducted to finalise the timestep selection and it was found that 100 timesteps per one complete mating ring revolution satisfy all flow-induced features and solver-based numerical requirements. Convergence is typically achieved within each timestep after 50 iterations and residuals are reduced by at least three orders of magnitude. Finally, steady-state converged simulations act as initial conditions for the dynamic analyses allowing transient simulations to start from a stable condition.

4. BOUNDARY CONDITIONS

The transient flow field is investigated for three rotational speeds, 50%, 75% and 100% N and air supply pressures of p/p_{ref} : 1, 1.5 and 2, where p_{ref} is the lowest pressure. Therefore, a rotating wall is imposed on the mating wall interface within the gas film while the rest of the walls are treated as no-slip stationary walls. The air is modelled as an ideal gas and pressure boundary conditions are used for the inlet and outlets, where atmospheric pressure is prescribed to the latter. The flow is adiabatic and the geometry is axisymmetric thus, a 30° sector is modelled with conformal rotational periodicity being imposed to the appropriate interfaces of the domain.

5. TRANSLATIONAL AND TILTING PERIODIC MOTION MODELLING

The dynamic behaviour of the seal involves the movement of the primary ring in both positional and angular directions. Initially, the seal is at the equilibrium position and then an oscillatory motion is induced with an amplitude of 1 μm for 15 complete periods. The capability to move the primary walls to

Copyright © 2025 by ASME;
reuse license CC-BY 4.0

explore realistic dynamic operations is developed using a novel implementation of imposed wall motion. A transfer function that controls the wall position is specified for the primary ring walls. During the translational motion, the displacement of the primary ring follows a cosine profile, as seen in Figure 3. Essentially, the primary ring is considered to act as a reciprocating piston, where its position is calculated using the following equation:

$$x_p = \sqrt{(r_c + L)^2 - x_{offset}^2} - r_c cos(\theta_c) - \sqrt{L^2 - \left(r_c sin(\theta_c) + x_{offset}\right)^2} \quad (1)$$

where x_p is the primary wall position, r_c the equivalent crank radius, L is the connecting rod length, θ_c is the crank angle and x_{offset} is the piston offset. The primary walls' location is updated every timestep in differential, gradual steps that correspond to 0.5 deg of crank angle step size. The frequency of this periodic motion follows a typical realistic oscillatory behaviour based on the investigated conditions.

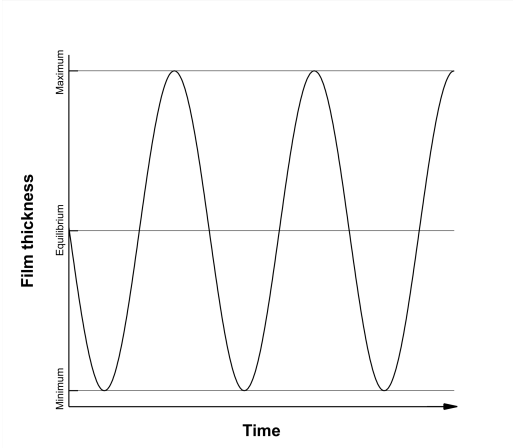


FIGURE 3: FILM THICKNESS DURING TRANSLATIONAL MOTION OF PRIMARY RING WALLS.

Apart from axial displacements, the DGS motion involves angular moments where the primary ring rotates causing the film gap to take different shapes as the primary ring and mating ring walls are not parallel. The angular displacement is prescribed to a fixed pivot point, which is located above the channel walls, and the motion of the walls is controlled based on the deviation angle created when the walls are not parallel. A maximum deviation angle is determined so that the entanglement of walls is avoided. The tilting motion of the geometry is seen in Figure 4 and the displacement of the primary walls, which follows a similar cosine profile, is implemented by the following equation:

$$\theta_{dev} = \theta_{max}\ \omega\ cos(\omega t) \quad (2)$$

In both displacement operations, the updated location of the walls is dealt with by the surface mesh elements of the discretized domain. After the walls' movement, the motion is transferred to the internal volume mesh. The motion of mesh nodes is controlled by a spring-based mesh deformation method in which mesh nodes are connected to each other with idealised springs. Before any boundary motion, the initial node spacings are assumed to be in equilibrium and a displacement at the wall nodes will generate a

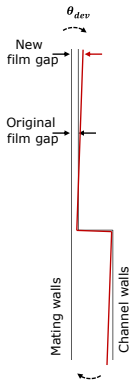


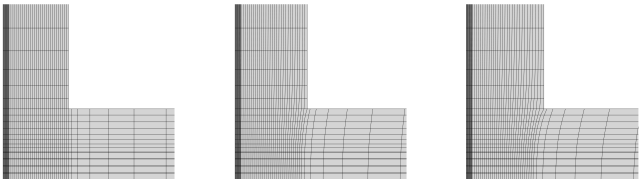
FIGURE 4: SCHEMATICS SHOWING THE ANGULAR MOTION OF THE PRIMARY WALLS.

force proportional to the displacement of all connected springs. The spring force is calculated by Hook's law and the spring stiffness, which is a constant, has been calibrated using a factor of 0.05.

$$\vec{F}_i = \sum_j^{n_i} k_{ij} \left(\Delta\vec{x}_j - \Delta\vec{x}_i\right) \quad (3)$$

$$k_{ij} = \frac{k_{factor}}{\sqrt{\left|\vec{x}_i - \vec{x}_j\right|}} \quad (4)$$

Additionally, boundary layer smoothing iterations are applied to improve the mesh quality and aggressive quality criteria thresholds, representative of rotating flows, are met. This approach allows the nodes of the first cells of the moving walls to have the same displacement vector as the ones on the wall. The effect of the combined approach is seen in Figure 5 highlighting the preservation of grid quality at three axial displacements.



(a) compressed position **(b) equilibrium position** **(c) extended position**

FIGURE 5: GRID EVOLUTION SHOWING THE MESH DEFORMATION DEPICTED AT THREE AXIAL LOCATIONS DURING TRANSLATIONAL MOTION.

The developed mesh deformation strategy was implemented after a mesh tracking routine, in which mesh quality criteria were probed and examined at each timestep, showed that the grid quality remains high for the entire period in both motions. The sufficient number of elements along with the small gradual step deformation eliminate the need to remesh the domain during the transient calculations while mesh folding is avoided too. This leads to ensuring that the mesh quality remains high throughout the calculations and that non-physical numerical artifacts emanating from the grid motion are removed.

Copyright © 2025 by ASME;
reuse license CC-BY 4.0

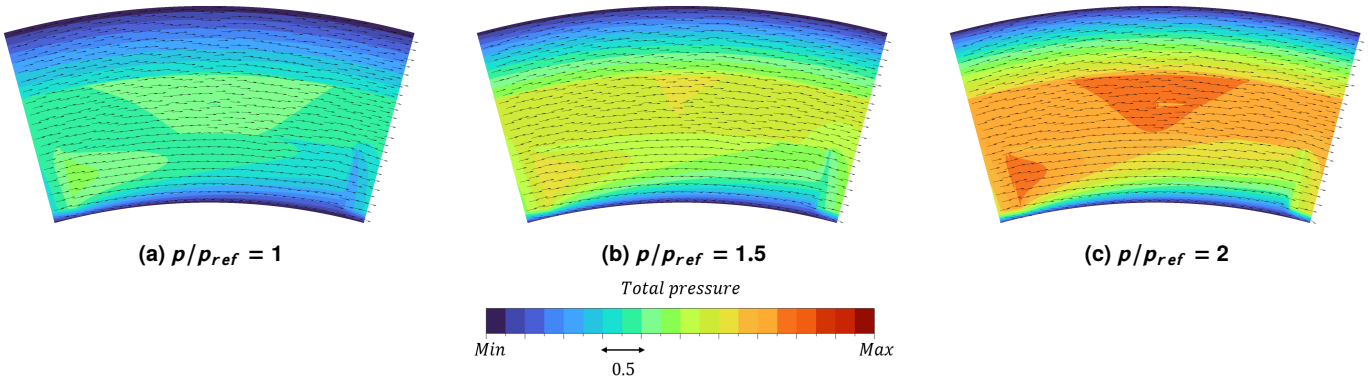


FIGURE 6: TOTAL PRESSURE CONTOURS AT THE MIDDLE OF THE GAS FILM FOR THREE DIFFERENT AIR SUPPLY PRESSURES IN A FIXED ROTATIONAL SPEED.

6. RESULTS & DISCUSSION

To completely characterise the dynamic behaviour of the DGS during the positional and angular displacement, the results are discussed in the following order:

1. The flow field in the gas film is characterised for different air supply pressures and rotational speeds using the Rayleigh pad configuration. At these conditions, the calculation of stiffness coefficients, which are strongly affected by the mating ring's rotational speeds and inlet pressure, is undertaken.

2. The effect of the primary ring's periodic axial displacement is described for a specified frequency at different rotor speeds and air supply pressures. Such axial vibrations are ubiquitous in non-contacting seals and have a detrimental effect on the operating stability of the seal. Therefore, the dynamic response of the investigated DGS is determined in terms of axial stiffness and damping coefficients. Transient analyses are conducted to provide the values of dynamic coefficients.

3. The effect of the primary ring's angular displacement is discussed for the same frequency at different rotor speeds and air supply pressures. This type of oscillation shows the response of the seal when a force is induced radially and cross stiffness and damping coefficients are computed based on a pivot point that is located closer to the outer radius. The dynamic coefficients are obtained for all investigated conditions and indicate the dynamic behaviour of the seal.

4. A rotordynamics model is developed to study the dynamic response of the system using the obtained linearised coefficients from CFD simulations. The vibration characteristics of the system are identified from a modal analysis.

6.1 Gas film flow field

The periodic motions of the primary ring are investigated at different air supply pressures and rotor speeds. The effects of these variables on the gas film flow field are described in this section. Figure 6 shows the total pressure contours in the middle of the gas film at three air supply pressures and a fixed rotational speed of 75% N. The black arrows show the direction of the flow, which is predominantly circumferential following the mating ring rotation. In all cases, the air is supplied through the orifice and expands on a pumping volume surrounded by the channel walls. The total pressure is high in this volume due to the higher mass flows and it decreases as the fluid moves radially into the film gap and out of the domain at atmospheric pressure. This shows that the channel walls entrap most of the air and the role of the smaller film gap is to decrease the mass flow in these regions, thus providing lower leakages and increasing the film stiffness. An increase in total pressure is noticed in the left Rayleigh pad as the flow moves into the small film gap creating a higher local pressure zone. The opposite phenomenon is noticed in the right Rayleigh pad where the total pressure decreases as the flow leaves from the film gap and expands, making it lose momentum. As expected, the total pressure increases with the air supply pressure causing a larger mass flow of air into the DGS along with a higher opening force and axial stiffness.

The effect of the mating ring rotational speed is shown in Figure 7 following a similar strategy. As the mating wall rotates faster, the circumferential velocity of the flow increases thus the velocity gradient inside the gas film is higher, leading to higher shear stresses. This affects the dynamic behaviour of the DGS as the opening force and film stiffness increase. The results show that the increase in total pressure is an order of magnitude higher when the air supply pressure rises compared to the increase in shaft rotational speed. During the tilting motion, in which the primary walls are rotated at a fixed pivot point, a similar flow topology is present with the pressure fields exhibiting local discrepancies in magnitude at the minimum and maximum deviation angles. Therefore, the flow field description in these conditions follows identical trends and is not included in the discussion.

6.2 Periodic Translational Motion

The dynamic response of the DGS as it is displaced axially for different rotational speeds and air supply pressures is discussed in detail in this section. Firstly, the axial stiffness (K_{xx}) coefficients are computed by steady-state simulations for various film thicknesses based on an equilibrium position at all investigated conditions. Figure 8 shows the variation of opening force

Copyright © 2025 by ASME;
reuse license CC-BY 4.0

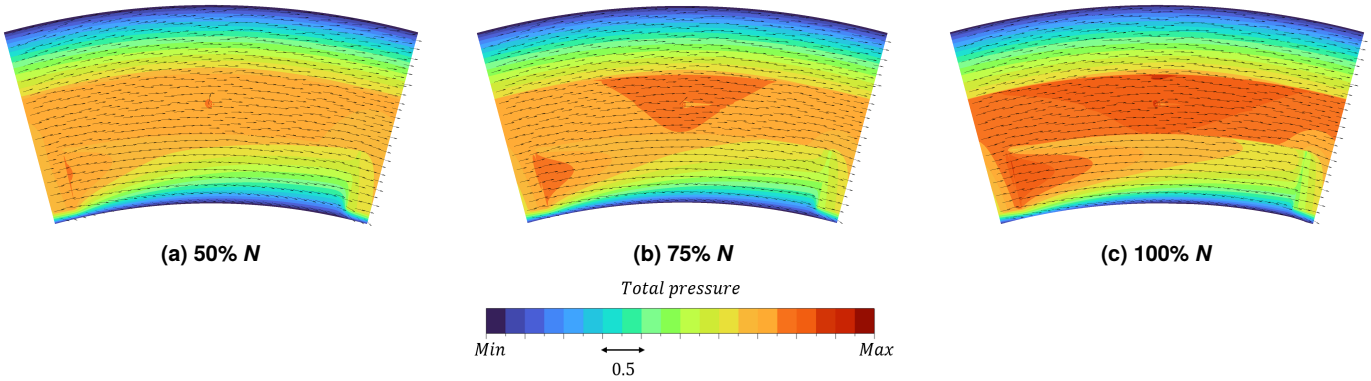


FIGURE 7: TOTAL PRESSURE CONTOURS AT THE MIDDLE OF THE GAS FILM FOR THREE DIFFERENT ROTATIONAL SPEEDS IN A FIXED AIR SUPPLY PRESSURE.

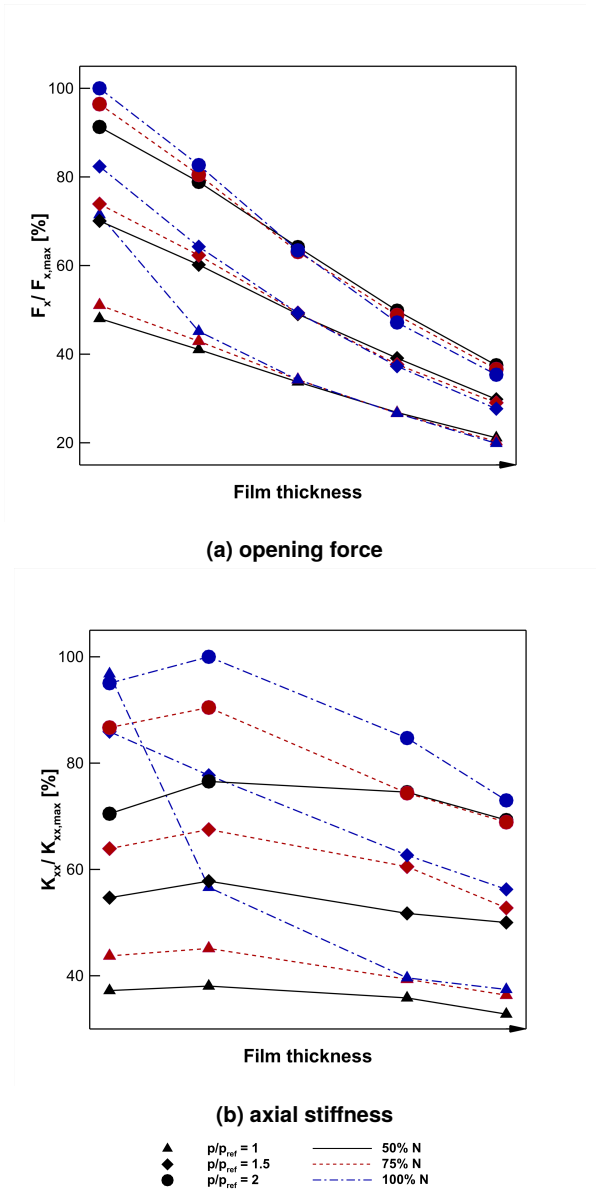


FIGURE 8: OPENING FORCE (A) AND AXIAL STIFFNESS COEFFICIENT (B) FOR DIFFERENT FILM THICKNESS VALUES

and K_{xx} with film gap thickness at different rotational speeds and air supply pressures. The values are normalised using the maximum value of the corresponding variable and the axial stiffness is computed using equation 5. The opening force and K_{xx} decrease as the film thickness increases with the latter exhibiting a small increase when the film thickness increases from its minimum size to a higher value. The displacement magnitude from the equilibrium location and the difference of $F_{x,p} - F_{x,eq}$ lead to the obtained behaviour. The opening force drop as the film thickness increases is calculated to be 60%, 40% and 30% for an air supply pressure of p/p_{ref} 2, 1.5 and 1 respectively. Both variables increase with the mating ring's rotational speed due to the higher dynamic pressure and shear stresses. A larger increase is noticed when the air supply pressure rises because of the higher air mass flow that is directed into the seal causing higher gas film pressure values. A peak of film stiffness at the minimum film thickness size is noticed at $p/p_{ref} = 1$ and 100% N. This sharp 35% increase is explained by the significant pressure rise at this rotational speed, which is caused by the larger shear stresses in combination with the small film thickness size.

$$F_{x,p} - F_{x,eq} = K_{xx}\Delta x \tag{5}$$

After the calculation of the axial stiffnesses, transient simulations are utilised to compute the damping coefficients. The total pressure flow field at three dynamic locations is seen in Figure 9 in a meridional plane showing the region that comprises the film gap and the channel walls. As expected, the total pressure drops when the gas film thickness increases for the same rotational speed and air supply pressure. This occurs because the flow expands and the effective pressure decreases causing a drop in the opening force.

The primary ring motion is the key driving factor to the damping response of the DGS. During the dynamic positional displacement, the primary walls move with varying speed according to their prescribed position, as shown in Figure 3. This motion yields damping forces and when the primary ring passes through the equilibrium position, the axial stiffness is zero. The damping coefficients were calculated using eq. 6 and the K_{xx} values at different film thicknesses other than the equilibrium one come from the steady-state simulations. Figure 10 shows the

Copyright © 2025 by ASME;
reuse license CC-BY 4.0

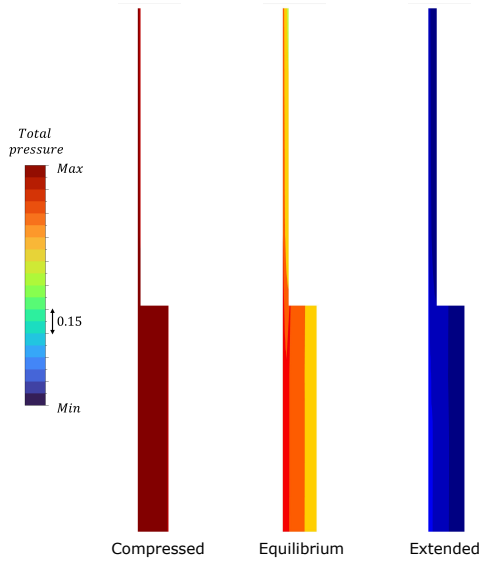


FIGURE 9: TOTAL PRESSURE FLOW FIELD AT THREE DYNAMIC PRIMARY WALL LOCATIONS FOR A FIXED ROTATIONAL SPEED AND AIR SUPPLY PRESSURE.

axial damping coefficient at the equilibrium location for different rotational speeds and air inlet pressures. The first observed trend is that the damping coefficient increases with the air supply pressure. The seal accommodates higher air mass flow rates from the larger inlet pressure leading to an increase in C_{xx}. Moreover, it is noticed that the damping coefficient decreases at the two lowest pressures as the rotational speed gets higher, agreeing with the findings of [19]. The increased air inlet pressure in combination with the higher rotational speed makes the damping of the system larger, which leads to better energy dissipation characteristics.

$$F_{x,p} - F_{x,eq} = K_{xx}\Delta x + C_{xx}\dot{\Delta x} \tag{6}$$

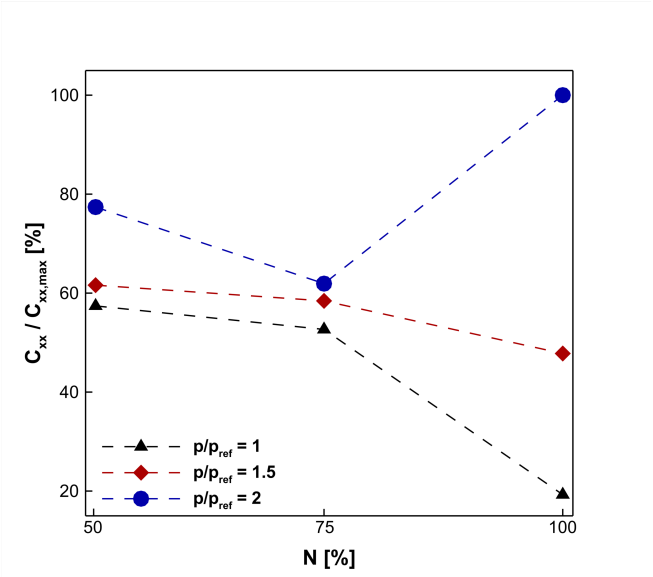


FIGURE 10: AXIAL DAMPING COEFFICIENT FOR DIFFERENT ROTATIONAL SPEEDS AND AIR SUPPLY PRESSURES.

Figure 11 shows the opening force for different rotational speeds and air supply pressures and is averaged over the last several periods. The opening force is directly dependent on the film thickness, hence its cosine profile, and increases with the air supply pressure and the rotational speed. At 100% N, when the film thickness is at its smallest size and starts expanding, the force is at its maximum and starts dropping. However, a small increase is noticed as the primary wall moves towards the equilibrium position. This occurs because the entrapped flow inside the pumping volume expands and moves radially outwards creating high local pressure zones in the gas film. The biggest force delta is approximately 60%, 50%and 40% at p/p_{ref} of 2, 1.5 and 1, respectively.

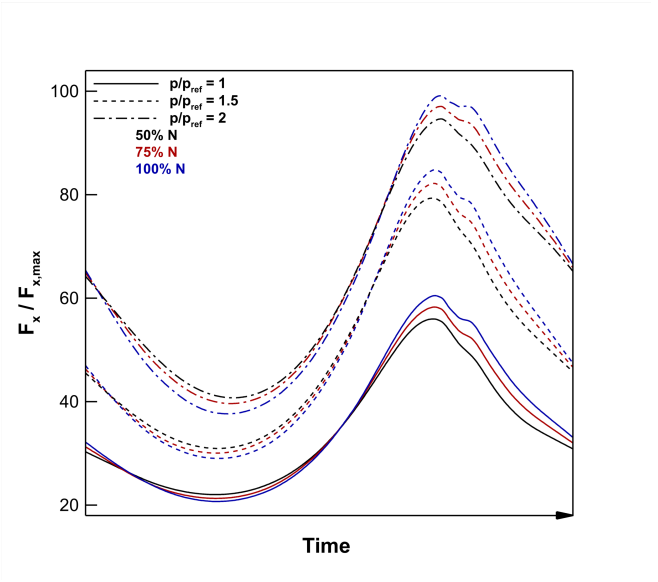


FIGURE 11: DYNAMIC AVERAGED OPENING FORCE FOR DIFFERENT ROTATIONAL SPEEDS AND AIR SUPPLY PRESSURES.

6.3 Periodic Tilting Motion

Angular oscillations are present during the dynamic operation of a DGS and the tilting motion around a fixed pivot point is discussed in this section. The flow field features are similar to the translational motion with local differences being noticed due to the angular movement of the primary ring. This motion induces forces in the vertical and horizontal directions and the cross stiffness coefficients (K_{xy}, K_{yx}) are calculated from several steady-state equations where the primary ring is pivoted between the maximum and minimum deviation angle. Then, transient analyses provide the means of calculating the cross damping coefficients (C_{xy}, C_{yx}). The cross stiffness coefficients are calculated based on the following equations:

$$K_{xy} = \frac{(F_{x,p} - F_{x,eq}) - K_{xx}\Delta x}{\Delta y} \tag{7}$$

$$K_{yx} = \frac{(F_{y,p} - F_{y,eq}) - K_{yy}\Delta y}{\Delta x} \tag{8}$$

The cross damping coefficients are computed using the following

Copyright © 2025 by ASME;
reuse license CC-BY 4.0

expressions:

$$C_{xy} = \frac{(F_{x,p} - F_{x,eq}) - K_{xx}\Delta x - K_{xy}\Delta y - C_{xx}\dot{\Delta x}}{\dot{\Delta y}} \quad (9)$$

$$C_{yx} = \frac{(F_{y,p} - F_{y,eq}) - K_{yy}\Delta y - K_{yx}\Delta x - C_{yy}\dot{\Delta y}}{\dot{\Delta x}} \quad (10)$$

where K_{yy} and C_{yy} are very close to zero because the induced force in the y direction due to the small displacement in the same direction is extremely low. Similarly, the fluid force on the x axis when the primary ring tilts and moves on the y direction is negligible leading to very low K_{yx} and C_{yx} coefficients. The contribution of these coefficients are negligible and are not included in the discussion.

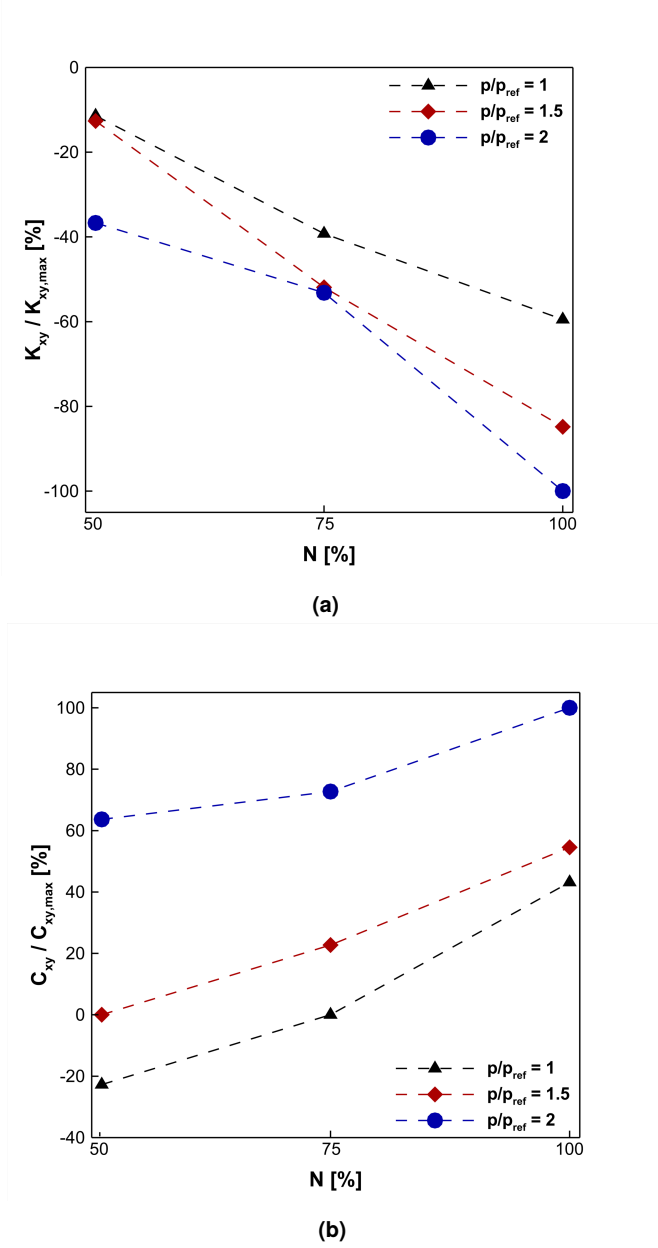


FIGURE 12: CROSS STIFFNESS AND DAMPING COEFFICIENTS AT DIFFERENT ROTATIONAL SPEEDS AND PRESSURES.

Figure 12 shows the normalised cross stiffness K_{xy} and damping coefficient C_{xy} over three rotational speeds at different air supply pressures and are normalised using the corresponding maximum values. The negative values indicate that the induced force is in the opposite direction to the displacement. In terms of rotor dynamics, this is interpreted as the force being applied to the direction of whirl and tangential to the whirl orbit. The K_{xy} reduces further as the air supply pressure increases while the C_{xy} becomes positive for the two highest pressure values. The rotational speed increase causes an increase in absolute values where the cross stiffness coefficient decreases and the damping coefficient increases. The negative K_{xy} values are disadvantageous because film instabilities are encouraged leading to rotor stability loss [20].

Figure 13 shows the normalised F_x forces averaged for the last few periods at different mating ring rotational speeds and air supply pressures. The F_x is the predominant force and its profile is directly dependent on the primary ring tilting movement where it is maximum when the gas film thickness is minimum. At this position, the forces converge to a similar value regardless the air inlet pressure as the shear stresses drive the pressure rise in the gas film. Following the same trends as in the translational motion, F_x increases with the air supply pressure while the force difference at a constant pressure increases during one period for higher rotational speeds due to the higher leakages. It is highlighted that the induced F_y is very low and therefore, its contribution, along with the associated damping coefficients, is considered negligible.

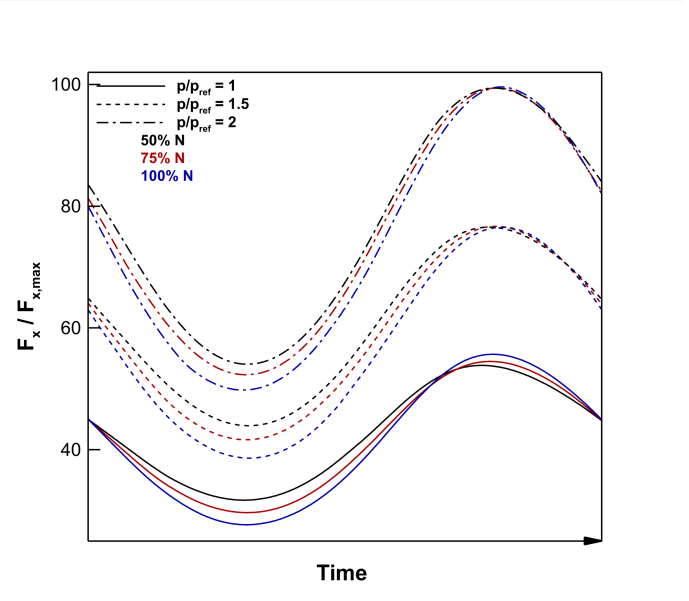


FIGURE 13: DYNAMIC F_x FOR DIFFERENT ROTATIONAL SPEEDS AND AIR SUPPLY PRESSURES DURING THE TILTING MOTION.

6.4 Simplified Rotordynamics Model

After the determination of the dynamic characteristics of the seal and the calculation of all linearised stiffness and damping coefficients, a rotordynamics model is developed to obtain the dynamic response of a system with the thin gas film providing

Copyright © 2025 by ASME;
reuse license CC-BY 4.0

the stiffness and damping forces. The simplified model is based on the well-known Jeffcott rotor and comprises of a flexible shaft and a rigid disc placed at the middle of the shaft. The mass of the system is concentrated in the disc and bearings support the two ends of the shaft. The dynamic gas film characteristics are applied to the bearings and the system is not constrained in any axis.

Figure 14 shows the Campbell diagram of the system for the first eight modes. The first few modes in the rotordynamic analysis correspond to rigid body motion, in which no rotor deformations are present. These modes typically have zero natural frequencies because they represent movements like translation and rotation of the entire rotor without any internal strain. As the rotor speed increases, the centrifugal forces rise making the system stiffer. Since stiffness is directly proportional to the natural frequency of the system, higher modes have a higher frequency. The excitation frequency is displayed by a dashed line and two critical speeds are obtained, the first one being at 57% of N and the second at 69%. Therefore, if the rotor operates above 55% N, the DGS must provide sufficient stiffness and damping in order to ensure that the system remains stable.

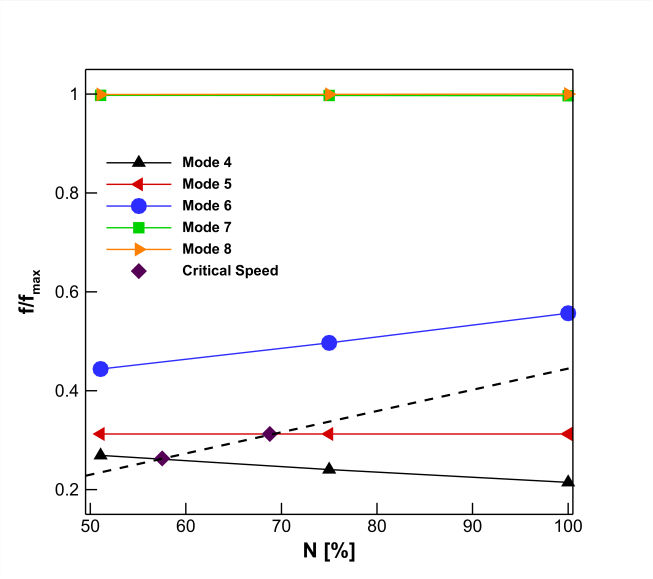


FIGURE 14: CAMPBELL DIAGRAM OF SIMPLIFIED MODEL.

7. CONCLUSION

A novel computational methodology that allows the physical movement of the primary ring inside the domain has been developed and is utilised to characterise the dynamic response of the seal during a positional and translational motion. The effects of the mating ring's rotational speed and air supply pressure have been investigated and the obtained linearised dynamic coefficients have been applied to a simplified rotordynamics model to capture its dynamic response. The key findings from this study are:

1. The increase in air supply pressure and shaft speed is observed to cause an increase in gas film total pressure mainly in the pumping volume and Rayleigh pads regions, where the air is entrapped. The role of Rayleigh pads in providing dynamic pressure is highlighted where higher local pressure zones are obtained when the flow moves to the smaller film gap.

2. During the translational primary ring motion, the axial stiffness and opening force reduce as the gas film thickness increases. It is observed that the decrease is steeper at higher air supply pressures, while higher stiffness values are obtained for higher shaft speeds at a constant pressure. The damping coefficient increases with the air inlet pressure but decreases at higher rotational speeds for low pressures. The transient opening force is directly dependent on the position of the ring and an unsteady phenomenon is captured that causes the local increase in force at a specific primary ring position.

3. When the primary ring tilts, the induced force in the y direction is extremely low and thus, the damping effect is negligible. Negative coefficients are obtained that adversely affect the stability of the seal and higher air supply pressures exacerbate the K_{xy} stiffness but improve C_{xy} damping coefficient. The averaged transient opening force exhibits the same profile as in the translational motion and the maximum opening forces converge to the same level for different rotor speeds at a constant air supply pressure. This occurs when the film gap size is the smallest and large shear stresses drive the gas film behaviour.

4. All dynamic coefficients obtained from CFD simulations are applied to a simplified rotordynamics model that provides insights into the dynamic characteristics of a rotor. Two critical speeds were obtained and the DGS must provide sufficient stiffness and damping effects to ensure that the rotor operates within enough stability margins if it is desired to operate at higher shaft speeds passing through these two modes.

This study addresses an important aspect of the operation of non-contacting seals in capturing their dynamic characteristics accurately without the need for taking into account analytical approaches. Therefore, the work provides methodological approaches that can be used as a design aid and to determine seal performance under dynamic condition. Moreover, investigations of a hitherto unexplored angular motion of the stationary ring provide useful insights into the realistic operating conditions that seals are exposed to to ensure long-term stable operation.

ACKNOWLEDGMENTS

The authors would like to thank John Crane for supporting this research and for permission to publish thne paper. Special thanks to Mr. Jasper Oranje and Dr. David Pickens of John Crane for comments and suggestions.

REFERENCES

[1] Zhou, Jianfeng. "Characteristcs of fluid film in optimized spiral groove mechanical seal." *Chinese Journal of Mechanical Engineering - CHIN J MECH ENG* Vol. 20 (2007). DOI 10.3901/CJME.2007.06.054.

Copyright © 2025 by ASME;
reuse license CC-BY 4.0

[2] Cich, Stefan D, Twist, Christina, Sihra, Inderpal and Taher, Matt. "Introduction to Dry Gas Seals and Systems." *Proceedings of the 49th Turbomachinery Symposium*. 2020. Turbomachinery Laboratory, Texas A&M Engineering Experiment Station.

[3] Zirkelback, Nicole. "Parametric Study of Spiral Groove Gas Face Seals." *Tribology Transactions* Vol. 43 No. 2 (2000): pp. 337–343. DOI 10.1080/10402000008982349.

[4] Ruan, Bo. "Finite Element Analysis of the Spiral Groove Gas Face Seal at the Slow Speed and the Low Pressure Conditions — Slip Flow Consideration." *Tribology Transactions* Vol. 43 No. 3 (2000): pp. 411–418. DOI 10.1080/10402000008982357.

[5] Bing, Wang and Huiqiang, Zhang. "Numerical Analysis of a Spiral-groove Dry-gas Seal Considering Micro-scale Effects." *Chinese Journal of Mechanical Engineering* Vol. 24 No. 1 (2011): pp. 146–153.

[6] Brunetiere, Noe¨ l, Tournerie, Bernard and Freˆ ne, Jean. "Influence of fluid flow regime on performances of non-contacting liquid face seals." *J. Trib.* Vol. 124 No. 3 (2002): pp. 515–523.

[7] Heshun, Wang and Cichang, Chen. "Numerical simulation on the geometric parameters of spiral grooved dry gas seals." *2009 ISECS International Colloquium on Computing, Communication, Control, and Management*, Vol. 2: pp. 5–8. 2009. IEEE.

[8] Heshun, Wang, Weibing, Zhu, Qiang, Wang, Zepei, Huang and Chening, Zhang. "Numerical simulation on flow field of spiral grooved dry gas seals." *2010 International Conference On Computer Design and Applications*, Vol. 5: pp. V5–227. 2010. IEEE.

[9] Yang, Zehai, Luo, Dan and Huang, Diangui. "Research on a transonic supercritical carbon dioxide centrifugal turbine." *Journal of Nuclear Engineering and Radiation Science* Vol. 5 No. 4 (2019): p. 041202.

[10] Badykov, Renat R and Falaleev, Sergey V. "Advanced dynamic model development of dry gas seal." *Procedia Engineering* Vol. 176 (2017): pp. 344–354.

[11] Chen, Yuan, Jiang, Jinbo and Peng, Xudong. "Gas film disturbance characteristics analysis of high-speed and high-pressure dry gas seal." *Chinese Journal of Mechanical Engineering* Vol. 29 No. 6 (2016): pp. 1226–1233.

[12] Chen, Yuan, Jiang, Jinbo and Peng, Xudong. "Dynamic characteristics and transient sealing performance analysis of hyperelliptic curve groove dry gas seals." *Tribology International* Vol. 116 (2017): pp. 217–228.

[13] Shahin, Ibrahim, Gadala, Mohamed, Alqaradawi, Mohamed and Badr, Osama. "Three dimensional computational study for spiral dry gas seal with constant groove depth and different tapered grooves." *Procedia Engineering* Vol. 68 (2013): pp. 205–212.

[14] Wang, Bing, Zhang, Huiqiang and Cao, Hongjun. "Flow dynamics of a spiral-groove dry-gas seal." *Chinese Journal of Mechanical Engineering* Vol. 26 No. 1 (2013): pp. 78–84.

[15] Badykov, Renat, Falaleev, Sergei, Wood, Houston and Vinogradov, Alexander. "Gas film vibration inside dry gas seal gap." *2018 Global Fluid Power Society PhD Symposium (GFPS)*: pp. 1–6. 2018. DOI 10.1109/GFPS.2018.8472383.

[16] Roache, Patrick J., Ghia, Kirti N. and White, Frank M. "Editorial Policy Statement on the Control of Numerical Accuracy." *Journal of Fluids Engineering* Vol. 108 No. 1 (1986): pp. 2–2. DOI 10.1115/1.3242537.

[17] Brunetiere, Noe¨ l. "A modified turbulence model for low Reynolds numbers: application to hydrostatic seals." *J. Trib.* Vol. 127 No. 1 (2005): pp. 130–140.

[18] ANSYS Inc. *ANSYS Fluent User's Guide, Release 2023R1* (2023). URL https://www.ansys.com.

[19] Ding, Xuexing, Lu, Junjue, Zhang, Weizheng and Zhai, Xiao. "Test analysis of gas film stiffness and system damping of spiral groove dry gas seal." *2016 13th International Conference on Ubiquitous Robots and Ambient Intelligence (URAI)*: pp. 279–287. 2016. IEEE.

[20] Shahin, Ibrahim, Gadala, Mohamed, Alqaradawi, Mohamed and Badr, Osama. "Centrifugal Compressor Spiral Dry Gas Seal Simulation Working at Reverse Rotation." *Procedia Engineering* Vol. 68 (2013): pp. 285–292. DOI https://doi.org/10.1016/j.proeng.2013.12.181.

Copyright © 2025 by ASME;
reuse license CC-BY 4.0



https://dspace.org/

A framework for computational dynamic characterisation of dry gas seals for assessing system response

Vitlaris, Dimitrios; John, Jerry Thomas; Santhanakrishnan, Mani Sekaran; Rajendran, David John; Roumeliotis, Ioannis ...

2025-06-16
American Society of Mechanical Engineers (ASME)
https://doi.org/10.1115/gt2025-153967
Vitlaris D, John JT, Santhanakrishnan M, et al., (2025) A framework for computational dynamic characterisation of dry gas seals for assessing system response. In: Proceedings of the ASME Turbo Expo 2025: Turbomachinery Technical Conference and Exposition, 16-20 Jun 2025, Memphis, Tennessee, USA, Volume 8: Structures and Dynamics — Bearing & Seal Dynamics; Emerging Methods in Engineering Design, Analysis and Additive Manufacturing; Fatigue, Fracture & Life Prediction; Probabilistic Methods; Rotordynamics, Article number GT2025-153967

Downloaded from a DSpace repository. https://dspace.org/